RSC Advances

PAPER

View Article Online
View Journal | View Issue

Cite this: *RSC Adv.*, 2023, **13**, 26392

Streamlined synthesis of potential dual-emissive fluorescent silicon quantum dots (SiQDs) for cell imaging

Di Sun, [a] Steven Wu, [ab] Jeremy P. Martin,[c] Kirati Tayutivutikul,[c] Guodong Du, [a] Colin Combs,[d] Diane C. Darland *[c] and Julia Xiaojun Zhao *[a]

One of the current challenges of working with nanomaterials in bioapplications is having a tool that is biocompatible (non-toxic) and produces stable, intense fluorescence for bioimaging. To address these challenges, we have developed a streamlined and one-pot synthetic route for silicon-based quantum dots (SiQDs) using a hydrothermal method. Part of our unique approach for designing the SiQDs was to incorporate (3-aminopropyl) triethoxysilane (APTES), which is an amphipathic molecule with hydroxyl and amine functional groups available for modification. In order to reduce the toxicity of APTES, we chose glucose as a reducing agent for the reaction. The resulting SiQDs produced potent, stable, potential dual-emissive fluorescence emission peaks in the visible and near-infrared (NIR) ranges. Both peaks could be used as distinguishing fluorescence signals for bioimaging, separately or in combination. The physical and optical properties of the SiQDs were determined under a range of environmental conditions. The morphology, surface composition, and electronic structure of the SiQDs were characterized using high resolution-transmission electronic microscopy (HR-TEM), energy dispersive X-ray spectroscopy (EDS), Fourier-transform infrared spectroscopy (FT-IR), X-ray powder diffraction (XRD) and X-ray photoelectron spectroscopy (XPS). The stability of the SiQDs was evaluated under a wide range of pHs. The biocompatibility and imaging potential of the SiQDs were tested in microvascular endothelial cells (MVEC), neural stem cells (NSC), and RAW 264.7 macrophage cells. The images obtained revealed different subcellular localizations, particularly during cell division, with distinct fluorescence intensities. The results demonstrated that SiQDs are a promising, non-toxic labeling tool for a variety of cell types, with the added advantage of having dual emission peaks both in visible and NIR ranges for bioimaging.

Received 31st May 2023
Accepted 27th July 2023

DOI: 10.1039/d3ra03669c

rsc.li/rsc-advances

1. Introduction

Fluorescence labeling plays an important role as a common reliable and visualization tool for biological research.[1,2] Conventional fluorescent materials are widely used as fluorescent probes or labels,[3,4] often including organic dyes (such as fluorescein or rhodamine) and fluorescent proteins (visible spectrum emitters). Although these fluorescent materials have been widely commercialized, challenges with photostability and surface modification often limit their performance in bioimaging.[5,6] In particular, when studying subcellular localizations and cell division processes, strong, stable, and small fluorescence labeling materials are necessary. Further, for imaging tissues and some biological samples, near infrared (NIR) fluorescence labels are critical. Compared to fluorescence emission in the ultraviolet/visible spectrum (UV/vis) region, the NIR fluorescence range exhibits less light scattering and, thus, deeper penetration of biological samples.[7–9] In addition, biological samples contain less auto-fluorescence in the NIR region than the UV/vis region. Therefore, photostable NIR fluorescent materials may be favorable for bioimaging, in some applications, to reduce sample autofluorescence and deepen penetration for inner structure observation.

In order to overcome limitations of conventional fluorescent materials, fluorescent nanomaterials have been extensively studied and applied in biomedical research over the last two decades.[1] Among these various fluorescent nanomaterials, quantum dots (QDs) have demonstrated optical properties that are advantageous, including photostability, high quantum yield, and size-dependent fluorescence emissions.[10,11] QDs are small, semiconductor nanoparticles that are a few nanometers in diameter and that confine the motion of the conduction band,

[a]*Department of Chemistry, University of North Dakota, Grand Forks, ND, 58202, USA. E-mail: julia.zhao@und.edu*

[b]*Department of Chemistry, University of South Dakota, Vermillion, SD, 57069, USA*

[c]*Department of Biology, University of North Dakota, Grand Forks, ND, 58202, USA. E-mail: diane.darland@und.edu*

[d]*Department of Biomedical Sciences, School of Medicine and Health Sciences, University of North Dakota, Grand Forks, ND, 58202, USA*

valence band, or excitons in all three spatial directions, with all three directions directly affecting the QDs' optical properties.[12,13] The QDs can exhibit unique optical and electronic properties,[14] such as strong fluorescence intensity, photostability, in addition to size-dependent and tunable fluorescence emission wavelengths.[15,16] QDs are generally, although not exclusively, made from heavy metals, such as cadmium selenide (CdSe) and cadmium telluride (CdTe). However, the toxicity of heavy metal based QDs can be a concern in biological systems and less toxic alternatives would be of value in bioimaging.[4,5,17–20]

Silicon (Si) has been used to generate a wide range of nanomaterials. The advantages of using Si include the fact that it is non-toxic and abundant in nature.[21] Thus, Si is a potential candidate for making QDs. At present, several synthesis methods for SiQDs have been established, including reduction of anhydrous Si compounds[22–24] and decomposition of a silicon-based precursor.[25–33] Recently, a new type of all-inorganic Si nanocrystals has been developed, and the Si nanocrystals with boron (B) and phosphorus (P) shells exhibited stable optical properties, working in aqueous solutions, both in the visible and NIR ranges.[4,26,34–36] Veinot's group reported a thermal disproportionation strategy using hydrogen silsesquioxane (HSQ) as a precursor to develop red-emitting fluorescent SiQDs through etching with hydrofluoric acid and linking with organic molecules.[30,37,38] The SiQDs product obtained with this method has pure Si without any other elements, including nitrogen (N), oxygen (O) and carbon (C) inside of the Si core. The resulting pure SiQDs are able to emit in the NIR range.[30,37,38] However, one major limitation is that most of the reported synthetic approaches are cumbersome, often generating toxic byproducts that might not be suitable for biological applications. Some of these methods require high-temperature calcination (1100–1300 °C) and hydrofluoric acid etching is often a necessary process to generate the SiQDs.

To lower the synthetic temperature and avoid a multi-step synthetic processing approach, we designed a streamlined method to synthesize SiQDs. The high temperature calcination step is not needed in the entire synthesis process. The reaction is rapid, utilizes a green chemistry approach, and does not require hazardous chemicals. The synthesis was completed through a simple pyrolysis method that uses (3-aminopropyl) triethoxysilane (APTES) in a glucose/water solution. Most importantly, the SiQDs produced showed potential dual-emissive fluorescence peaks in the visible and NIR regions. The SiQDs generated were characterized by various analytical and imaging methods to determine the consistency and quality of the synthesis approach and the final product. Finally, the SiQDs were successfully applied to imaging with primary cultures of mouse-brain-derived microvascular endothelial cells (MVEC), primary embryonic mouse neural stem cells (NSC), and the human monocyte/macrophage-like cell line RAW 264.7 to determine their bioimaging potential.

2. Experimental section

2.1 Materials

(3-Aminopropyl) triethoxysilane (APTES), D-glucose, 2-[4-(2-hydroxyethyl) piperazin-1-yl] ethanesulfonic acid (HEPES buffer, 99.5%), 3-(cyclohexylamino)-propanesulfonic acid (CAPS buffer, ≥99%), 2-(cyclohexylamino) ethanesulfonic acid (CHES buffer, ≥99%), maleic acid (≥99%), citric acid (≥99.5%), quinine sulfate, IR-775 chloride and penicillin-streptomycin were purchased from Sigma Aldrich (St. Louis, MO, USA). A Spectra/Por® standard regenerated cellulose pre-treated dialysis membrane with a molecular weight cut-off (MWCO) of 1 kilo dalton (kDa) was purchased from Spectra Laboratories (Rockleigh, NJ, USA). Deionized (DI) water (18 mΩ cm @ 25 °C) was used in the experiments. Primary cultures of mouse-brain-derived microvascular endothelial cells (MVEC) derived from CD1 adult mouse brain were purchased from Cell Biologics (Chicago, IL, USA). Primary neural stem cells (NSC) cultures were microdissected from embryonic day (E) 13.5 mouse dorsal anterior forebrain based on approved IACUC protocols. NSCs were enriched using SSEA1 antibody enrichment with Dyna-Bead magnetic beads. The RAW 264.7 cell line was purchased from the American Type Culture Collection (ATCC, Manassas, VA, USA). Fetal bovine serum (FBS) was purchased from Peak Serum (Wellington, CO, USA). Dulbecco's modified Eagle medium (DMEM), Neurobasal medium, N2 and B27 supplements, Electron Microscopy Sciences (EMS) 16% paraformaldehyde aqueous solution, phosphate buffered saline (PBS, 1×), cell culture plates, 8-well chambered cover glass w/ non-removable wells, 96-well plates, propidium iodide, Alexa Fluor 488 phalloidin, the Live/Dead Cell Imaging Kit, and Invitrogen CyQUANTTM Lactate Dehydrogenase (LDH) Cytotoxicity Assay kit were purchased from Thermo Fisher Scientific (Waltham, MA, USA). The immunolabeling block solution was prepared in the lab as previously described.[39,40] The Vectashield hardset mounting medium was purchased from Vector Laboratories (Burlingame, CA, USA). Lab-Tek II 8-well Chamber Slides were purchased from Nalgene-Nunc International Corp (Naperville, IL, USA). Micro cover glass was purchased from Sargent-Welch VWR Scientific (Buffalo Grove, IL, USA). The cell counting system used the LUNA-II Cell Counter from Logos (Biosystems, Annandale, VA).

2.2 Instrumentation used for morphological and optical characterization of SiQDs

A Hitachi 7500 transmission electron microscope (Hitachi, Tokyo, Japan) and a high-resolution transmission electron microscope (HR-TEM) JEOL JEM-2100 (Jeol, Tokyo, Japan) were used to observe the morphology of SiQDs. The energy dispersive X-ray spectroscope (EDS) from Oxford Instruments (Concord, MA, USA) attached to the Hitachi SU8010 scanning electron microscope (SEM) (Hitachi, Tokyo, Japan) was used to determine elemental distribution. A Rigaku Smartlab-3KW X-ray diffractometer (XRD) (Wilmington, MA, USA) was used to determine the crystalline structure of the SiQDs. A K-Alpha X-ray photoelectron spectrometer (XPS) from Thermo Fisher Scientific (Waltham, MA, USA) was applied to determine the binding energies and identify the elements in the SiQDs. The infrared spectroscopy analysis was conducted using a Thermo Fisher Nicolet iS5 FT-IR spectrometer (Waltham, MA, USA). Malvern Nano-ZS Zetasizer (Malvern Panalytical, UK) was used to

measure the hydrodynamic diameters and the zeta potential of the SiQDs. The fluorescence spectra and photostability measurements were obtained using a Shimadzu RF-6000 spectrophotometer (Shimadzu, Tokyo, Japan). A Horiba Fluorolog JobinYvon fluorophotometer 3 (Chicago, IL, USA) was used for recording NIR fluorescence spectra of the SiQDs. UV-visible absorption studies were performed using a PerkinElmer Lambda 1050 UV-Vis-NIR spectrophotometer (Akron, OH, USA). A VWR Symphony vacuum oven with Teflon-lined stainless-steel autoclave reactors (Radnor, PA, USA) was used for synthesis of the SiQDs. An Olympus BX71WI inverted fluorescence microscope (Olympus, Center Valley, PA) was used for a live and dead cell imaging and immunolabel imaging. An Olympus FV3000 Laser Scanning Confocal Microscope (Olympus, Center Valley, PA) was used for the *in vitro* cell imaging of the SiQDs with different cell types. Cell viability through quantification of LDH was evaluated by BioTek ELx800 microplate reader (Winooski, VT, USA).

2.3 Preparation of potential dual-emissive SiQDs

The synthesis of SiQDs was performed using a modified hydrothermal method. Briefly, 0.450 g D-glucose as a reducing agent was dissolved in 8.0 mL nitrogen (N_2)-saturated water and stirred for 10 min at room temperature (RT). After the formation of a homogeneous reaction solution, 2.0 mL of APTES was injected into the nitrogen-saturated solution and stirred for 10 min. Then, the mixture was transferred into a Teflon-lined stainless steel autoclave oven and incubated at 200 °C for 8 h. The sample was naturally cooled down to room temperature (RT) and ultra-filtered (filter aperture: 0.10 μm) resulting in a dark red solution after the heating step. To remove unreacted materials including APTES and D-glucose at the end of the preparation, the 1 kDa Molecular Weight Cut Off (MWCO) Spectra/Por® standard regenerated cellulose pre-treated dialysis membrane was used to dialyze the SiQDs for 24 h against deionized (DI) water. The prepared solution was collected and stored at 4 °C prior to use and was stable for at least two months based on morphometrical and optical analyses.

2.4 Measurement of SiQDs photoluminescence quantum yield (PLQY)

The PLQY of SiQDs was calculated for visible (447 nm) emission using eqn (1) below with the quinine sulfate in 0.1 M H_2SO_4 as the visible standard reference. The NIR (844 nm) emission PLQY of SiQDs was calculated using the same eqn (1) below with the NIR I dye–IR775 chloride in methanol as the NIR standard reference.

$$\Phi_{\text{Sample}} = \Phi_{\text{Standard}}\left(\frac{\text{Grad}_{\text{Sample}}}{\text{Grad}_{\text{Standard}}}\right) \times \left(\frac{{\eta_{\text{Sample}}}^2}{{\eta_{\text{Standard}}}^2}\right) \quad (1)$$

Quinine sulfate in 0.1 M H_2SO_4 has been investigated as a visible emission range standard reference with Φ_{standard} of 54.0% with ${\eta_{\text{standard}}}^2$ being equal to 1 in the case of 0.1 M H_2SO_4.[41,42] IR775 as a NIR I dye has also been quantified, such that the QY at $\lambda_{\max}$ emission 792 nm is 7.0% in methanol.[43,44] Moreover, SiQDs would also have ${\eta_{\text{sample}}}^2$ equal to 1 when prepared in a pH 7.0 HEPES buffer. The PLQY of the two emission ranges were calculated to be 45.3% at visible emission range and 6.4% at NIR I emission range, compared with quinine sulfate in 0.1 M H_2SO_4 as a visible range standard reference and IR775 in methanol as a NIR I range standard reference, respectively.

2.5 Determination of SiQDs stability

The stability of SiQDs was determined across a range of pHs, including the optimal pH for cell culture (7.0). A buffer with different pHs was prepared using 20 mM maleic acid, citric acid, HEPES, CHES, or CAPS buffer with final pH steps of the series, including: 1, 3, 5, 7, 9, and 11. The maleic acid buffer was used to prepare the pH 1 solution, the citric acid buffer was used to prepare the pH 3 and 5 solutions, the HEPES buffer was used to prepare the pH 7 solution, the CHES buffer was used to prepare the pH 9 solution and CAPS buffer was used to prepare the pH 11 solution. The pH was adjusted by the addition of 1 M sodium hydroxide or 37% hydrochloric acid solutions, as needed. All solutions were maintained at a concentration of 0.5 mg mL^{-1} SiQDs.

2.6 Cell culture

Primary cultures of mouse-brain-derived microvascular endothelial cells (MVEC) were obtained from CD1 adult mouse brain and maintained in complete DMEM with 1× Glutamax and 4.50 g L^{-1} glucose supplemented with 10% fetal bovine serum, penicillin solution (100 U mL^{-1}), and streptomycin (100 μg mL^{-1}). The primary mouse neural stem cells (NSC) were maintained in complete Neurobasal medium with Glutamax (Gibco BRL), and 100 ng mL^{-1} of epidermal growth factor (EGF) supplemented with B27 (without vitamin A) and N_2 proprietary components (Gibco BRL/Fisher Scientific) as well as penicillin-streptomycin. A human macrophage cell line, RAW 264.7 cells, were also prepared and grown in complete DMEM. All cells were cultured at 37 °C under a humidified atmosphere of 5% CO_2. Cell counts for assay plating were determined by counting a diluted suspension with an EVE or LUNA-II automated cell counter using 0.4% trypan blue solution exclusion to distinguish and quantify live from dead cells.

2.7 *In vitro* biocompatibility and cell proliferation

To evaluate the *in vitro* biocompatibility, different concentrations of SiQDs (0, 25, 50, 100, 200, or 400 μg mL^{-1}) were evaluated using the Invitrogen™ LIVE/DEAD™ Cell Imaging Kit (488/570). The MVEC cells were incubated in a 24-well plate at a density of 10 000 cells per well. Various concentrations of SiQDs were added into each well and incubated at 37 °C under a humidified atmosphere of 5% CO_2 for 24 h. The labeling solutions from the LIVE/DEAD™ Cell Imaging Kit (LIVE green and DEAD red) were thawed immediately prior to use, and 1.0 mL of LIVE green solution was transferred into and mixed with DEAD red solution. An equal volume of the LIVE/DEAD solution mix was added to the cells and incubated for 15 min at RT. Afterwards, the toxicity effect of the SiQDs was determined using the LIVE/DEAD viability assay using

an inverted fluorescence microscope, per manufacturer's instructions, and the results quantified to compare across SiQDs concentrations.

The CyQUANT™ LDH colorimetric cytotoxicity assay kit was also used to quantify cellular cytotoxicity. Briefly, the RAW 264.7 cells were plated into a 96-well plate overnight. A gradient concentration of SiQDs (0, 2, 5, 10, 20, 50, 100, 200 and 500 μg mL^{-1}) was first added into the wells and incubated in a CO_2 incubator at 37 °C. After 24 h of incubation with a gradient concentration of SiQDs, 10 μL of sterile water was added into each of 3 replicate wells of 0 μg mL^{-1} group to serve as the spontaneous LDH release while 10 μL of 10× Lysis buffer was added into each of 3 replicate wells to serve as the maximum LDH controls. After 45 min of incubation, 50 μL aliquots of all groups were transferred into a new 96-well plate, mixed with 50 μL of the reaction mixture solution. After 30 min incubation at RT, protected from light, 50 μL of stop solution was added and the results quantified with ELx800 microplate reader set at 490 nm wavelength to determine the cell viability.

2.8 *In vitro* immunolabeling and imaging

The primary cultures of mouse-brain-derived MVEC and primary mouse NSC were cultured in 8-well Lab Tek Chamber slides at a target plating density of 2500 cells/well. After the cells adhered for 24 h, the SiQDs were added to the wells in concentrations ranging from 0–100 μg mL^{-1}. The cells were incubated with the SiQDs for 8 h to allow cellular uptake after which the media was removed, and the cells were washed with 1× PBS (with Ca^{2+} and Mg^{2+}) 3 times with 15 min for each wash. The cells were then fixed by adding 100 μL of 16% paraformaldehyde to the chamber wells that contained 300 μL of media with cells. The cells were fixed for 15 min at RT. The fix solution was removed, and the cells were washed one time with 1X PBS for 5 min. The cells were permeabilized with a block solution (3% donkey serum, 1% bovine serum albumin, 0.1% Triton X-100, 1× PBS with Ca^{2+} and Mg^{2+}) at RT for 30 min. Alexa Fluor 488 phalloidin (diluted 1 : 300 in block solution) was used to label the actin cytoskeleton and highlight the cytoplasmic contents of the cells. Nuclei were labeled with propidium iodide (diluted 1 : 2500 in block solution) which binds to the DNA. Cells were imaged using Olympus BX71WI inverted fluorescence microscope and images collected in each channel were postprocessed to generate composites using Photoshop (v. 2023).

Cell imaging of SiQDs was further investigated by labeling the RAW 264.7 cell line with 0, 50, 100, or 200 μg mL^{-1} of SiQDs onto cells plated in 8-well chamber slides. After 4 h incubation, the chamber slides were washed with 1× PBS 3 times for 15 min each and then fixed with 4% PFA for 15 min. After 3 additional PBS washes, the chambers were removed, and the slides were coverslipped with mounting medium and imaged using the Olympus FV3000 Laser Scanning Confocal Microscope.

3. Results and discussion

3.1 Rational design of the SiQDs

To develop a streamlined method for synthesis of fluorescent SiQDs, the focus of our rational design approach included four primary goals. The first goal was to determine an approach that would lower the synthetic temperature, thereby eliminating a need for high temperature calcination. The second goal was to avoid multi-step reactions to develop a simple and rapid synthesis method. The third goal was to utilize a green chemistry approach that eliminated hazardous chemical production in the synthesis process. The fourth goal was to develop an imaging tool that would be readily absorbed by a variety of cell types in culture. Based on these goals, the selection criteria for a suitable silicon precursor was critical. To this end, we researched various silicon precursors, finally selecting (3-aminopropyl) triethoxysilane (APTES) which is an amphipathic molecule with amine functional groups available for modification. We speculated that a simple and easy pyrolysis of APTES would result in SiQDs when a suitable reducing agent was present. In addition, when a pyrolysis reaction occurred, we predicted that APTES would produce non-toxic products of silicon/silica, amino-based silica and water with glucose

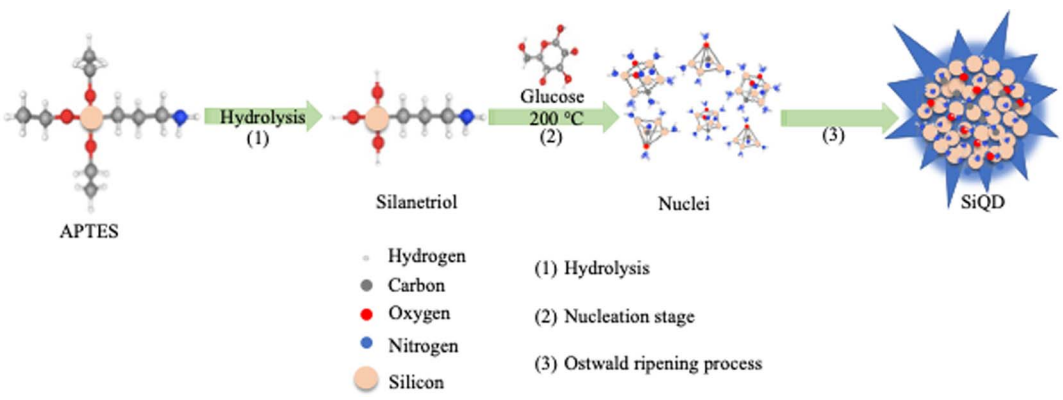

Fig. 1 Schematic diagram of the synthetic process for SiQDs using glucose as the reducing agent. Step (1) APTES was first hydrolyzed to form aminopropyl silanetriol. Step (2) Aminopropyl silanetriol was transformed into unstable nuclei during the nucleation stage under 200 °C and in the presence of the reducing agent, glucose. Step (3) In the Ostwald ripening process, small, unstable nuclei were easily adsorbed and desorbed to form stable dots with luminescence capacity.

utilized as a non-toxic effective reducing agent. Based on this rational design approach, we used APTES as a reactant for assembling SiQDs under a hydrothermal process as depicted in Fig. 1. First, as the reactive silane reagent, APTES, was subjected to hydrolysis in an aqueous solution. Aminopropyl silanetriol was quickly produced as a result (Fig. 1, step 1), which may further undergo condensation reactions to form Si–O–Si bonds. Then at elevated temperature, aminopropyl silanetriol was nucleated through reduction by glucose (Fig. 1, step 2). In the hydrophilic environment, species containing Si–O, Si–Si and Si–C bonds formed nanoparticle "seeds". As the reaction proceeded, these seeds developed into small crystal nuclei. During the formation of small nuclei, the process of Ostwald ripening occurred, and the nuclei grew with the deposition and absorption of small nanocrystals with large surface area-to-volume ratios and low stability. The end results of this reaction series were stable SiQDs production (Fig. 1, step 3).

3.2 Monitoring the formation of SiQDs during synthesis

The formation of SiQDs could be indirectly observed through monitoring the changes of solution color throughout the experimental process. Initially, the solutions were colorless when APTES was added into the glucose solution. During the synthesis process, the reaction solution was transferred into a Teflon-lined autoclave reactor and incubated at 200 °C for 8 h. The product was purified using MWCO of 1 kDa dialysis tubing for 24 h in DI water. After hydrothermal reaction, the color of the solution with glucose changed from colorless to red (Fig. 2A). The solution showed an intense blue color when viewed under hand-held illumination with UV light at an excitation wavelength of 365 nm (Fig. 2B). This suggested the formation of strong blue emitting SiQDs with glucose as the reducing agent. Control solutions that contained only APTES with DI water did not change color or form; further, no cohesive particles were generated after hydrothermal treatment for 8 h. HR-TEM images showed a clear lattice spacing of 0.31 nm corresponding to (111) plane of Si crystal (Fig. 2C), which was consistent with the bond angle results that have been reported for boron and phosphorous co-doped SiQDs.[34]

The size distribution and zeta potential were determined using DLS (Fig. 2D and E). The size of SiQDs ranged from 3 to 10 nm with an average diameter of 4.8 ± 0.5 nm. The positively charged zeta potential of 48.7 ± 1.3 mV was measured after 8 h of reaction, indicating that the SiQDs have no aggregatation.[45]

3.3 Characterization of synthesized SiQDs

The composition of the SiQDs was further analyzed using EDS, FTIR, XRD and XPS techniques. As shown in Fig. 3A energy-dispersive X-ray spectroscopy (EDS) spectrum confirmed the main components of silicon (Si) along with oxygen (O), carbon (C), and nitrogen (N) of the SiQDs. The inset panel displays the atomic ratio% of C, O, Si, and N. The copper (Cu) and chloride (Cl) values were from the SEM sample stage holder since Cu is the background with a small amount of Cl.

To identify surface functionalities surrounding the SiQDs, FTIR analysis was performed. The FTIR spectrum of SiQDs showed in Fig. 3B is in the range of 4000–600 cm^{-1}. The spectrum showed two broad peaks and one sharp peak at 3352 cm^{-1}, 3284 cm^{-1} and 1593 cm^{-1}, respectively, which may be attributed to N–H stretching vibration and N–H bending vibration. The two peaks at 3352 cm^{-1} and 3284 cm^{-1} are due to primary NH_2 groups of the SiQDs. The peak at 2922 cm^{-1} was assigned to the C–H stretching vibration. The peaks between the range of 1464 to 1230 cm^{-1} were attributed to vibrational scissoring and symmetric bending of Si–CH_2. The appearance of peaks at 1001 cm^{-1} and 688 cm^{-1} were attributed to Si–O–Si stretching vibration and bending vibration. These results confirmed the presence of primary amine functional groups on the surface of

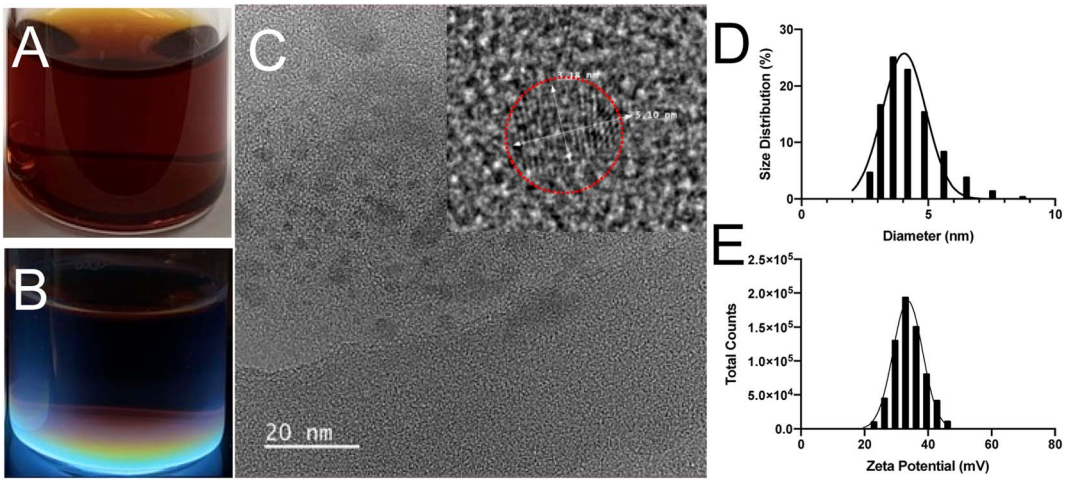

Fig. 2 Characterization of the SiQD nanomaterials. (A) and (B) Photographs are shown of the SiQDs under white light and UV light illumination, respectively. (C) HR-TEM image of the SiQDs is shown with the scale bar of 20 nm. The inset panel is a magnified image with a clear lattice space of a SiQD. (D) The hydrodynamic diameter of the SiQDs was measured by DLS and graphed as a size distribution across the quantified population of SiQDs. (E) The zeta potential of the SiQDs was measured by DLS with the total counts graphed across the mV range assessed. The results shown are representative of 3 independent preparations with similar results.

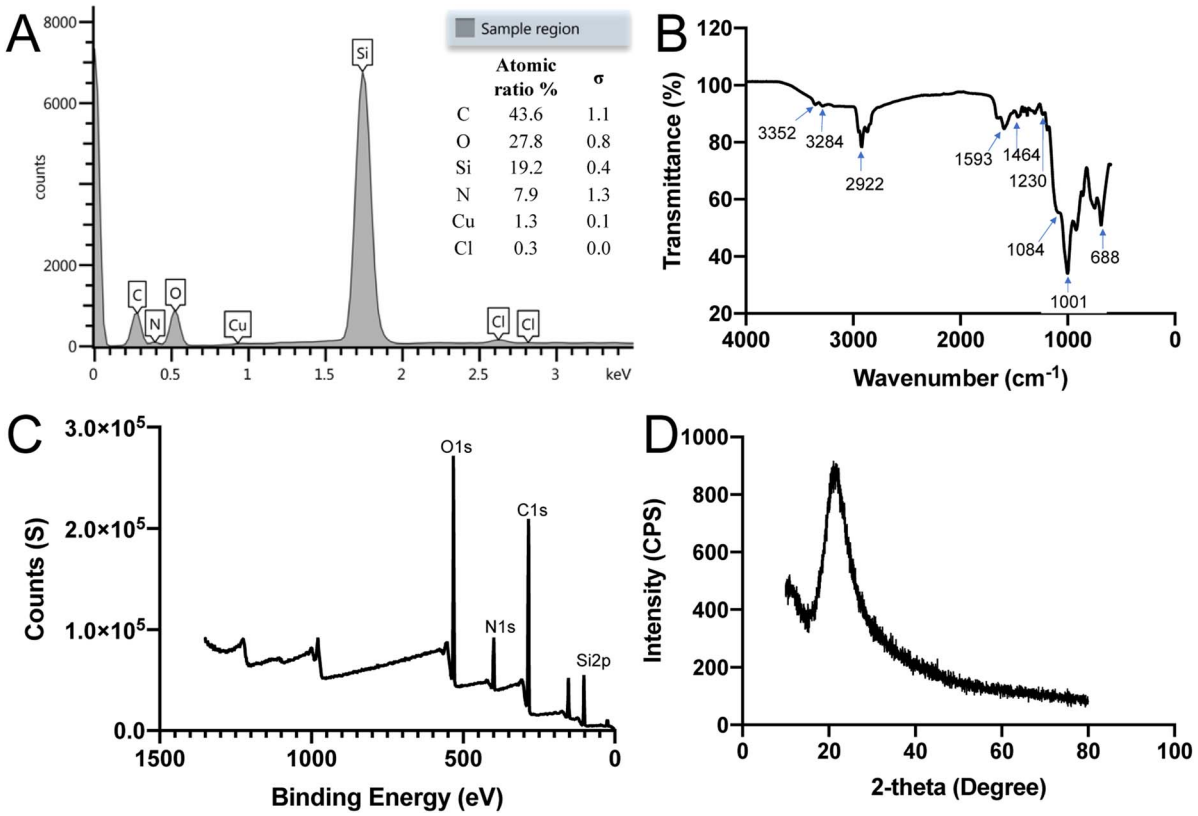

Fig. 3 Characterization of SiQDs' energy and diffraction patterns. (A) Energy-dispersive X-ray spectroscopy (EDS) spectrum. The graph depicts the mean energy of the X-ray (keV) relative to the counts. The inset panel displays the atomic ratio% of C, O, Si, N, Cu, and Cl, with the latter two elements present due to the stage coating. The EDS spectrum revealed the main components of C, O, Si and N. (B) FTIR spectrum of the SiQDs showed the existence of Si–O, Si–C, C–H, N–H bonds. Blue arrows indicate wavelength number for each bonds. (C) X-ray photoelectron spectroscopy (XPS) spectrum analysis of the SiQDs further verified existence of Si, O, C and N, and their different electronic states. (D) Powder X-ray diffraction (XRD) pattern assessment of SiQDs showed a broad band of signal with the θ peak at 21.06°.

potential dual-emissive SiQDs along with Si–O–Si and Si–C linkages. Hydrophilic primary NH_2 functional groups contribute to the water dispersibility of these SiQDs. Additionally, the intensity of an absorption band depends on the polarity of the bond, and a higher polarity bond will show a more intense absorption band.[46] Because of the non-polarity of the Si–Si bond, it is challenging to obtain a specific peak from FT-IR; however, the results described here were consistent with previously published work.[22,47,48] The FT-IR results highlight the strength and stability of the Si–C bond formed between the SiQDs and aminopropyl silanetriol as well as the Si–O surface bonds present.

The surface composition and electronic structure of SiQDs were further characterized by X-ray photoelectron spectroscopy (XPS) and X-ray powder diffraction (XRD). The full range XPS spectrum of SiQDs suggested that the SiQDs were composed mainly of oxygen (O), carbon (C), nitrogen (N) and silicon (Si) with four main peaks at binding energy values of O 1s (538 eV), C 1s (407 eV), N 1s (291 eV) and Si 2p (108 eV), respectively (Fig. 3C). In addition to the Si(0) oxidation state, Si(II) and Si(IV) were also present, resulting from attachment of nitrogen (N), carbon (C), and oxygen (O) containing species on the surface of SiQDs.[49] The XPS results were in accordance with the FTIR results. Fig. 3D gave the XRD pattern of SiQDs with a broad band distributed at 21.06°, indicating that the amorphous phase was formed. Based on the above results and our previous experience in synthesizing silicon-based nanomaterials, it is likely that some amorphous silica is formed on the surface of SiQDs.[50,51] Moreover, the XRD analysis is consistent with the reported results that show amorphous formation of SiQDs.[29]

3.4 Optical properties of potential dual-emissive SiQDs

Generally, Si based nanoparticles exhibit poor luminescent performance due to the indirect nature of the band gap transition. However, when the size of SiQDs was decreased comparable to or below the exciton Bohr radius of Si (~5 nm), the band gap increased and transitioned from indirect to direct due to the quantum confinement effect.[52,53] Eventually, the decreased SiQDs size (~4.8 nm) resulted in an enhancement of optical properties.

Fluorescence emission of the SiQDs produced was shown in Fig. 4A. The SiQDs had two broad emission peaks at 447 nm and 844 nm with the excitation set at 347 nm, indicating that the SiQDs could be used as a strong fluorescent label in both visible and NIR ranges. The fluorescence shown in Fig. 4A had been investigated for SiQDs and can be attributed to the Γ–Γ direct band gap transition and the fluorescent result was in good agreement with the previous report.[22,52,54] The NIR emission was speculated to be caused by the SiQDs core doped with small

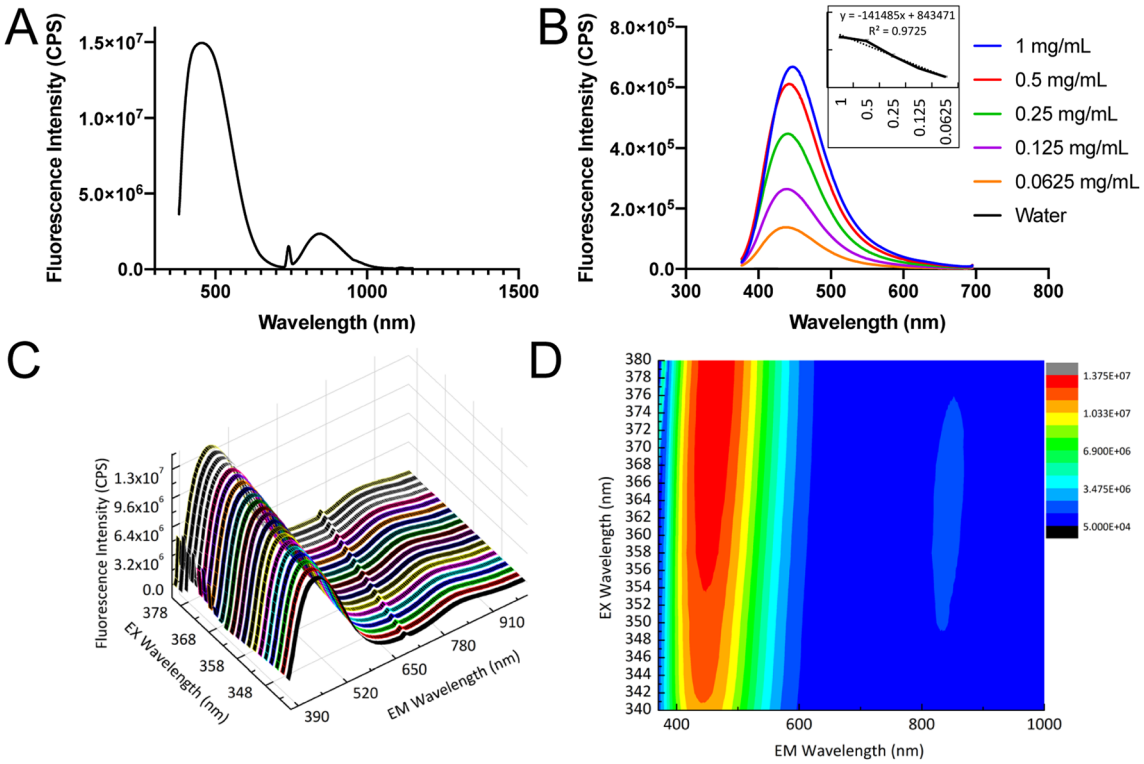

Fig. 4 The fluorescence properties of potential dual-emissive SiQDs. (A) The emission spectrum of SiQDs is shown. (B) The emission spectra are compared for different concentrations of SiQDs, showing the emission peak at 447 nm. The inset graph is the calibration curve of different concentrations of SiQDs under emission of 447 nm. (C) The 3D spectra of SiQDs are shown with varying excitation and emission wavelengths. (D) The fluorescence excitation-emission contour map of SiQDs shows two emission ranges in the map with the minor peak in the NIR range. The data interval was 1.0 nm, the scan speed was 6000 nm min^{-1}, and the slit width was 5 nm.

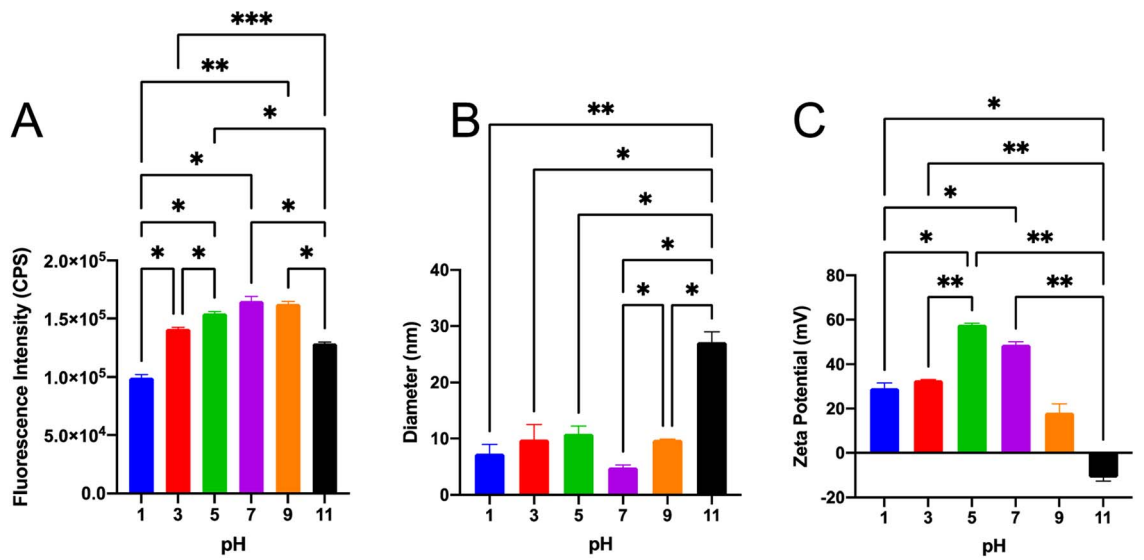

Fig. 5 Evaluation of fluorescence intensity and physical properties of SiQDs under a wide range of pH. (A) Evaluation of the fluorescence properties of SiQDs under a wide range of pH. The one-way ANOVA showed distinct differences comparing the fluorescence intensity under different pHs. (B) The hydrodynamic diameter of the SiQDs under a wide range of pH. The one-way ANOVA showed distinct differences–comparing the diameter under pH 11 relative to other pHs tested. (C) The Zeta potential of SiQDs was determined under a wide range of pH. The one-way ANOVA showed distinct differences–comparing the zeta potential under pH 11 to other pHs. Data were presented as the mean ± SD, $n = 3$. The pair-wise analysis with the Sidak multiple comparisons test showed significance with connecting bars indicating a comparison: $p < 0.05$ was presented as *, $p < 0.01$ was presented as **, $p < 0.001$ was presented as ***.

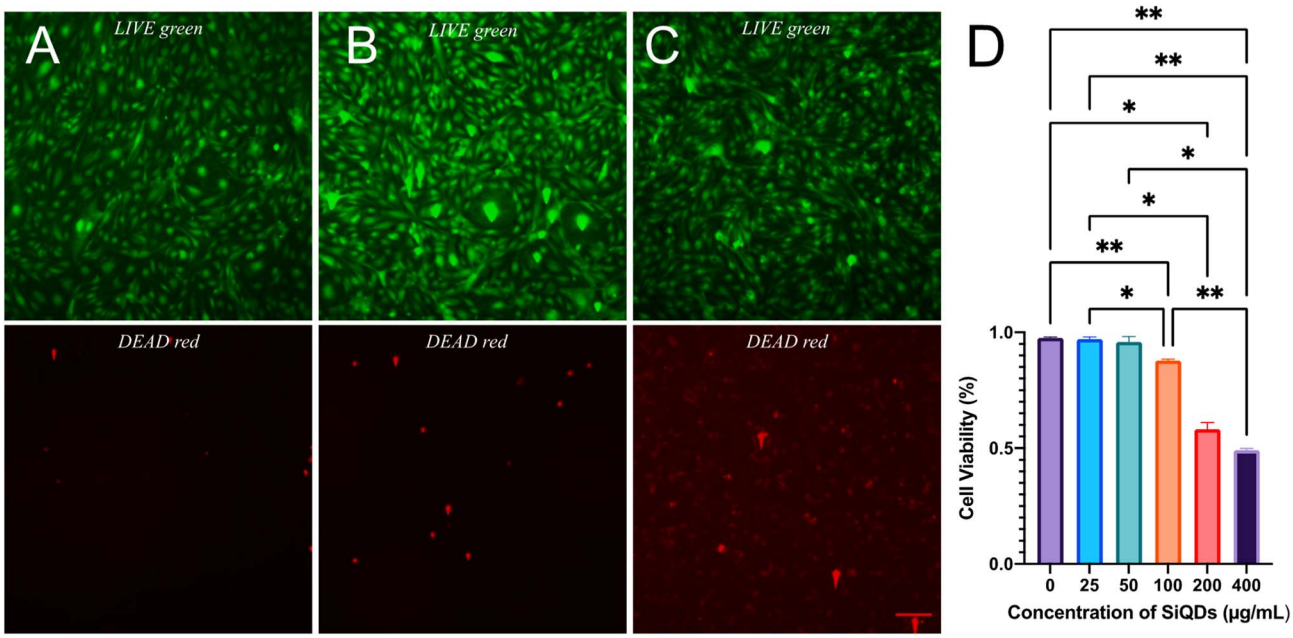

Fig. 6 Biocompatibility assessment of SiQDs on MVEC. Different concentrations of SiQDs (0, 25, 50, 100, 200, 400 μg mL^{-1}) were added to MVEC. (A–C) The fluorescence images of MVEC cells treated with SiQDs at 0, 50, and 400 μg mL^{-1}, respectively, are shown for the LIVE detection (green, top panels) and DEAD detection (red, bottom panels). (D) Cell viability of MVEC cells was assayed using an inverted fluorescence microscope. The cell viability percentage of untreated MVEC cells was used as control (0 μg mL^{-1}). Data were presented as the mean ± SD, $n = 3$. The one-way ANOVA showed distinct differences between 200, 400 μg mL^{-1} and other SiQDs concentrations. The pair-wise analysis with Sidak multiple comparisons test showed significance with bars indicating a comparison: $p < 0.05$ was presented as *, $p < 0.01$ was presented as **.

amounts of other elements, such as oxygen (O), nitrogen (N), and carbon (C) to form to form Si–O and Si–C bonds, which is considered trapping emission.[55,56]

The fluorescence intensity was proportional to the concentration of SiQDs and the intensity remained high even at the concentration of 0.0625 mg mL^{-1}. The calibration curve was calculated from different concentrations of SiQDs under blue emission at 447 nm (Fig. 4B). The 3D spectra confirmed two clear emission ranges, with the main blue emission ranging from 380–650 nm and the NIR emission ranging from 760–900 nm (Fig. 4C). The contour map and integral profile of the SiQDs excitation and emission spectra were shown in Fig. 4D, with the results consistent with the 3D spectra.

3.5 Effect of pH on fluorescence properties of SiQDs

To utilize SiQDs as a fluorescent label in bioimaging or biosensing, the pH tolerance of SiQDs is critical. The performance of SiQDs at different pHs, ranging from 1 to 11, was investigated (Fig. 5). The fluorescence intensity at different pHs was compared using the one-way ANOVA data analysis method (Fig. 5A). The fluorescence intensity dropped at pH value extremes (pH 1, 11) indicating that SiQDs were prone to fluorescence quenching under strong acidic and basic conditions. The SiQDs had the higher fluorescence intensity in the wide range of pH from pH 3 to pH 9, which brackets the pH optimal for biological applications.

The size distribution and zeta potential of the SiQDs at different pHs were also analyzed. There was no significant change in size distribution from pH 1–pH 7. The results showed that the average hydrodynamic diameter of SiQDs was no more than 11.0 nm in the range of pH 1–9. However, at pH 11 the hydrodynamic diameter increased to 27.1 nm, likely reflecting an agglomeration phenomenon in high alkaline environment (Fig. 5B).

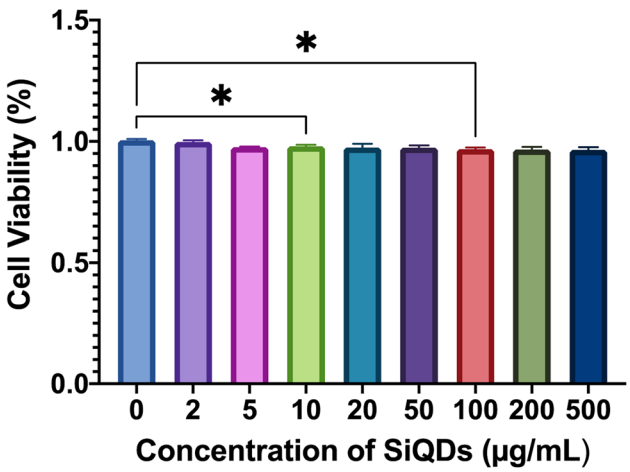

Fig. 7 Cytotoxicity analysis of SiQDs on RAW 264.7 cells. The cells were treated with a range of SiQDs from 0 to 500 μg mL^{-1} SiQDs and then tested for viability using the LDH assay. Data are presented as the mean ± SD, $n = 3$. The one-way ANOVA showed significant differences comparing 0 with 10 μg mL^{-1} and 0 with 100 μg mL^{-1}, although cell viability for all concentrations closely matched controls. The pair-wise analysis with Sidak multiple comparisons showed significance with bars indicating a comparison: $p < 0.05$ was presented as *.

If nanoparticles in solution have a large negative or positive zeta potential, then they will tend to repel each other and the nanoparticles will not aggregate.[45] In order to determine if there was a pH-dependent aggregation of the SiQDs, we determined the surface charge of the SiQDs under different pHs (Fig. 5C). The SiQDs had positively charged zeta potentials at all pH ranges, except pH 11. These were: pH 1, +29.2 mV; pH 3, +32.8 mV; pH 5, +57.8 mV; pH 7, +48.7 mV; pH 9, +18.2 mV. In contrast, the zeta potential was −11.2 mV at pH 11, which likely reflects aggregation at the strong basic pH. Overall, the SiQDs had a wide pH tolerance range from pH 3 to pH 7 and they avoided aggregation in the pH 3 to pH 7 solutions.

3.6 Evaluating biocompatibility of potential dual-emissive SiQDs

To evaluate the feasibility of SiQDs as a fluorescence agent for cell labeling, the cell viability in the presence of SiQDs was evaluated. The LIVE/DEAD Cell Imaging Kit was used to determine effect and response of MVEC cells treated with different concentrations of SiQDs. The live cells were distinguished by the intracellular esterase activity as determined by the enzymatic conversion of the non-fluorescent calcein AM to the fluorescent calcein. The dead cells were indicated by a bright red fluorescence which was generated by binding to DNA. The cell imaging kit is a sensitive two-color fluorescence cell viability assay optimized for FITC and Texas Red™ filters, allowing discrimination between live and dead cells with two probes that measure SiQDs for cytotoxicity and cell viability. The live cell detection component produces intense, uniform green fluorescence in live cells (ex/em 488 nm/515 nm). In contrast, the dead cell detection component produces predominantly nuclear red fluorescence (ex/em 570 nm/602 nm) in cells with compromised cell membranes, a feature that is correlated with cell death.

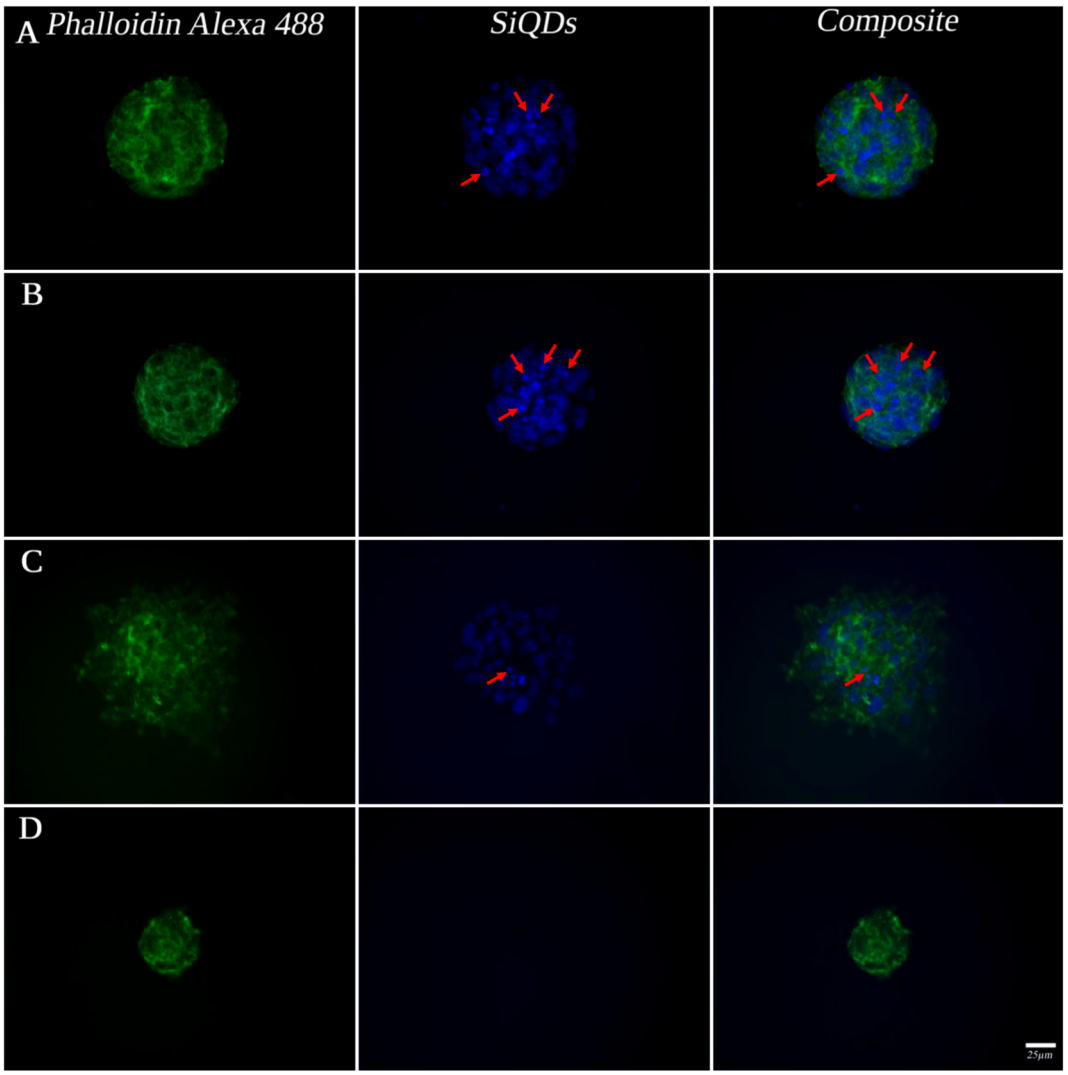

Fig. 8 Neural stem cell (NSC) labeling with SiQDs. NSC were grown in neurosphere culture and labeled with different concentrations of SiQDs and then post-fixation labeled with Alexa Fluor 488 phalloidin (green, actin). NSC were cultured in 8-well Lab Tek Chamber slides at a target plating density of 2500 cells/well. From (A) to (D): NSC incubated with SiQDs at 100 μg mL^{-1}, 50 μg mL^{-1}, 25 μg mL^{-1} and 0 μg mL^{-1} for 8 h. The scale bar is 25 μm. This experiment was repeated 3 times with similar results and a representative experiment is shown.

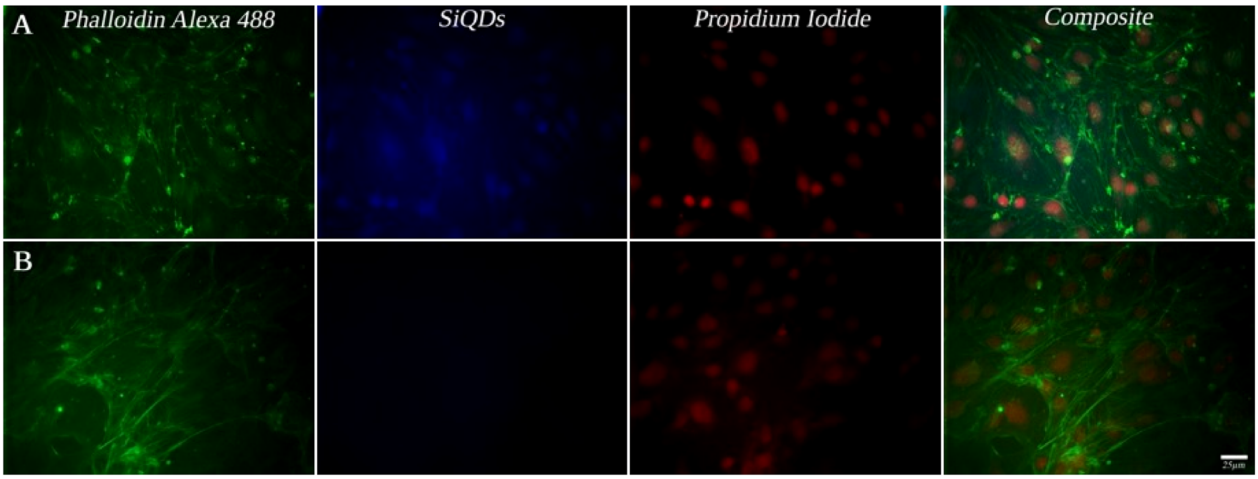

Fig. 9 Microvascular endothelial cells (MVEC) labeled with varying concentrations of SiQDs. MVEC were grown in monolayer culture and incubated with SiQDs after which they were post-fixed and labeled with PI (red, nuclei) and Alexa Fluor 488 phalloidin (green, actin). MVEC were cultured in 8-well Lab Tek Chamber slides at a target plating density of 2500 cells/well. MVEC were incubated with 50 μg mL^{-1} SiQDs (A) or 0 μg mL^{-1} SiQDs (B) for 8 h. The scale bar is 25 μm. This experiment was repeated 3 times with similar results and a representative experiment is shown.

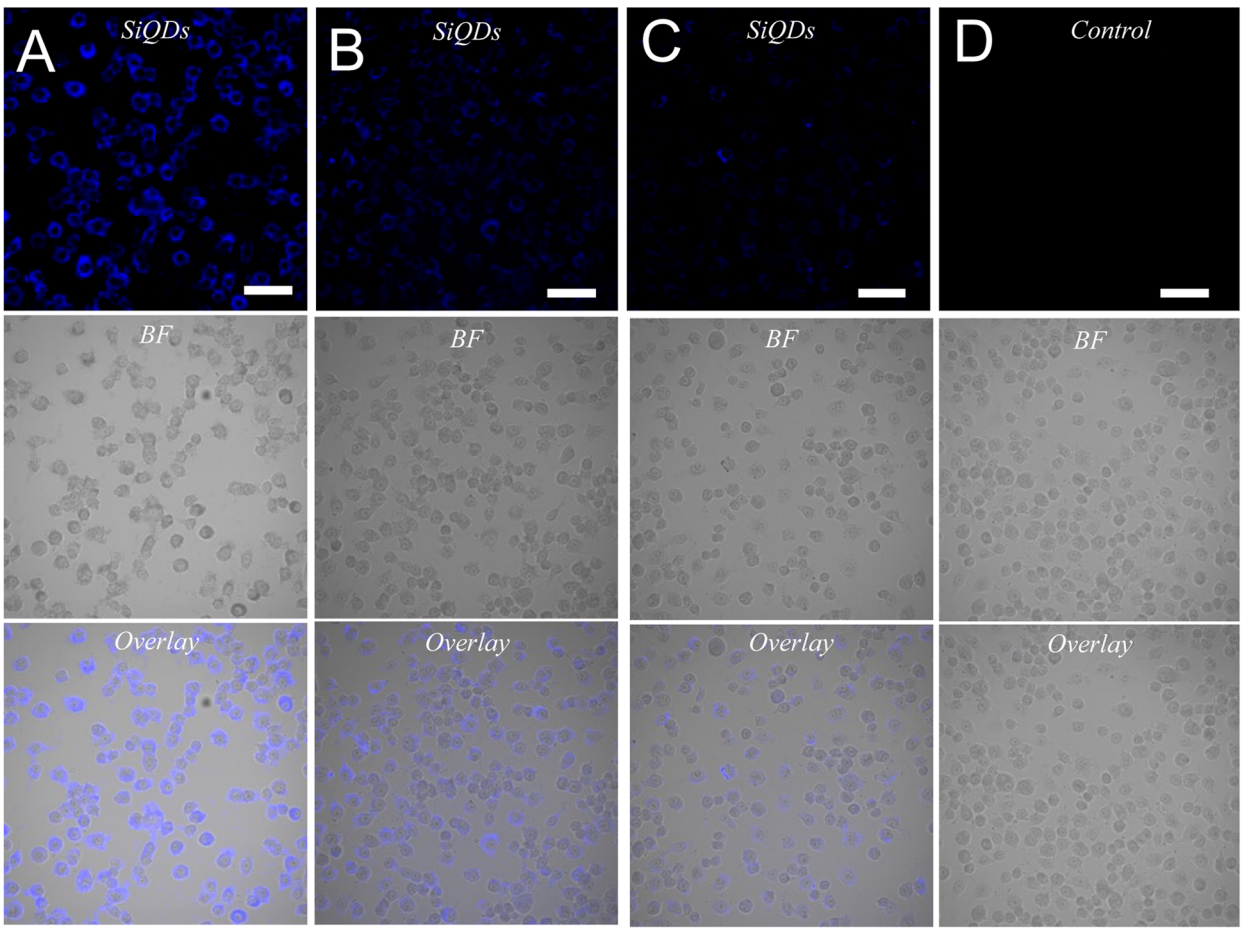

Fig. 10 RAW 264.7 cell labeling with varying concentrations of SiQDs. From (A) to (D): RAW 264.7 cells incubated with SiQDs at 200 μg mL^{-1}, 100 μg mL^{-1}, 50 μg mL^{-1} and 0 μg mL^{-1}, respectively, for 4 h. The cytoplasmic distribution of SiQDs (blue, top panels) is shown in comparison with brightfield imaging (BF, middle panels) and the overlay (bottom panels). The scale bar is 50 μm. This experiment was repeated 3 times with similar results and a representative experiment is shown.

Fig. 6 shows the results of MVEC cells treated with different concentrations of SiQDs. Fig. 6A–C are images of MVEC cells incubated with SiQDs at concentrations ranging from 0, 50 and 400 μg mL^{-1}, respectively. The top panels (A–C, green) showed the distribution of live cells, and the bottom panels (red images) indicate the dead cells imaged after ultraviolet (UV) illumination. The number of live cells and dead cells were counted using NIH ImageJ software.[57] The cells treated with SiQDs lower than 100 μg mL^{-1} displayed good viability compared with the cells treated with concentrations of 200 μg mL^{-1} SiQDs and 400 μg mL^{-1} SiQDs. The cell viability in 25 μg mL^{-1}, 50 μg mL^{-1} and 100 μg mL^{-1} was determined to be 97%, 96% and 88%, respectively (Fig. 6D). Obvious toxicity was observed when the concentration of the SiQDs was 200 μg mL^{-1} or higher. The percent of cell viability in 200 μg mL^{-1} and 400 μg mL^{-1} SiQDs was 58% and 49%, respectively. The results indicated that the SiQDs had good biocompatibility at 100 μg mL^{-1} in the MVEC.

Cell viability was further evaluated by LDH assay using a macrophage cell line (RAW 264.7). The results showed that there was negligible cytoxicity observed in the RAW 264.7 cells, for all ranges of SiQDs tested (Fig. 7). This result likely reflects the high tolerance of this macrophage cell line - RAW 264.7 cells to SiQDs. The cell viability results confirmed that the SiQDs can be further applied as a cell labeling agent with RAW cells. Comparing the tolerance of MVEC relative to RAW 264.7 cell line for SiQDs, the RAW 264.7 cell line shows minimal cytotoxicity impact. This result highlights the importance of testing multiple cell types for each preparation of SiQDs.

3.7 *In vitro* cell immunolabeling and imaging

While MVEC cell images provided a unique opportunity to test biocompatibility of the cell with SiQDs, stem cells have received increasing attention because of their capacity to differentiate into diverse tissue types and increase functional recovery. Additionally, the vascular endothelium is critical in regulating the interaction of circulating cells with the blood vessel wall. Vascular endothelial cell imaging provides information about the permeability of the vasculature and functional abnormalities of the vessels. To expand the type of cell that we tested for bioimaging, we next assessed the ability of the SiQDs to label primary neural stem cell (NSC). First, MVEC and NSC were treated with different concentration of SiQDs (0, 25, 50, 100 μg mL^{-1}) for 8 h after which unincorporated SiQDs were removed. The cells were fixed and imaged using an Olympus BX51WI fluorescence microscope. As shown in Fig. 8, the NSC cells incubated with 100 μg mL^{-1} of SiQDs showed strong blue fluorescence, reflecting the uptake of SiQDs. As the concentration of SiQDs used was decreased, the fluorescence intensity lessened. The NSC cells incubated without SiQDs had no blue fluorescence, as expected. In parallel, the cells were also labeled with Alexa Fluor 488 phalloidin to bind to the actin cytoskeleton in order to visualize the location of SiQDs in the cells. The MVEC cells that were incubated with the concentration of SiQDs at 50 μg mL^{-1} showed a similar cytoplasmic labeling pattern for the SiQDs as was observed with the NSC (Fig. 9). Immunolabeling results verified that the SiQDs were not toxic at less than 100 μg mL^{-1} and provided a robust signal, localized primarily in and around the nucleus and throughout the cytoplasm for both MVEC and NSC.

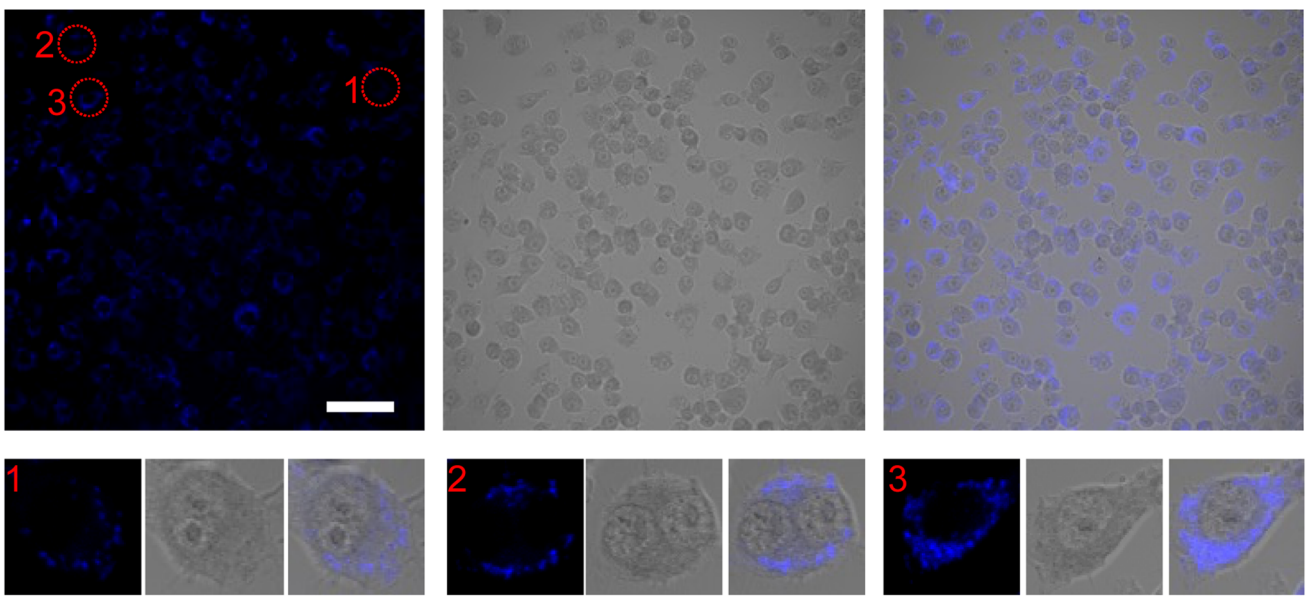

Fig. 11 Differential distribution of SiQDs in RAW 264.7 cells undergoing mitosis. The RAW 264.7 cells were labeled with 100 μg mL^{-1} of SiQDs for 4 hours, then fixed and imaged with a confocal microscope. The circles indicated (1, 2, 3) highlight different cell cycle stages of RAW 264.7 cells from prometaphase, end of mitosis, and the single cell, respectively, that are shown in higher magnification in the lower panels. The scale bar is 50 μm for the top panels. This experiment was repeated 3 times with similar results and a representative experiment is shown.

Interestingly, after 4 h incubation of RAW 264.7 cells with SiQDs, there was a different distribution of fluorescence signal compared with MVEC and NSC. Generally, SiQDs entered the cells and were distributed in the cytoplasm and excluded from the nucleus (Fig. 10). When cells were not undergoing mitosis, SiQDs accumulated in the cytoplasm away from the nucleus (Fig. 11). During prometaphase, SiQDs were distributed in small amounts in the cytoplasm of the cells. When the cells were at the end of mitosis, SiQDs began to be distributed at the sites of cytokinesis, dispersing away from the nucleus. The results showed retention and re-distribution of the SiQDs as the cytoplasm volume changed and redistributed during mitosis.

Overall, the SiQDs displayed emission in the visible blue range with no overlap with the other labeling agents, confirming this as a valuable and stable labeling tool for a wide range of cells.

4. Conclusions

In conclusion, we have developed a streamlined and simple synthetic route for the formation of potential dual-emissive SiQDs *via* the hydrothermal method using glucose as a reducing agent. This reaction process includes hydrolysis, nucleation, and Ostwald ripening steps. The SiQDs have abundant amine functional groups from the precursor APTES, and the SiQDs size ranges from 3 to 10 nm with positively charged zeta potential on the surface. The optical properties of the SiQDs yielded two distinct emission peaks at 447 nm and 844 nm, generated with only one excitation wavelength at 347 nm with the 447 nm wavelength being the most intense. The PLQY of two emission ranges were calculated to be 45.3% at visible emission range and 6.4% at NIR I emission range compared with quinine sulfate in 0.1 M H_2SO_4 and IR775 in methanol as standard references, respectively. While there are limitations associated with the excitation wavelength in the UV range, these SiQDs are valuable imaging tools for cell culture and can be readily used in combination with antibody immunolabeling reagents with compatible emission spectra. The *in vitro* imaging of NSC and MVEC with SiQDs revealed bright blue fluorescence with minimal toxicity at concentrations less than 100 $\mu g\ mL^{-1}$ and a clear distribution in the cytoplasm and the nucleus. The macrophage-like cells RAW 264.7 exhibited more pronounced uptake of the SiQDs compared with the NSC and MVEC cells, which is in line with the normal biological function of this phagocytic population. Once SiQDs entered the RAW 264.7 cells, however, the SiQDs were restricted to the cytoplasm. The distribution of SiQDs in the RAW 264.7 cells varied in different stages of cell division and the signal was displaced as cytokinesis ensued. It is important to note that the signal was retained post-division.

The biocompatible and nontoxic features of the SiQDs make these a valuable tool for bioimaging and biosensing. However, there are still many challenges that need to be resolved to fully realize the potential of this promising material. SiQDs are less than 10 nm in diameter and can easily aggregate under harsh environmental conditions that can affect the fluorescent properties of SiQDs, thereby weakening their biological applications.[58,59] Surface modification of SiQDs with other molecules or chemicals may offer a strategy to avoid aggregation and increase their applicability. Therefore, the conjugation of SiQDs with other biomolecules is a significant research direction in the future, supporting a wider bioapplication for SiQDs.

Author contributions

Di Sun: conceptualization, methodology, data curation, writing original draft, visualization, investigation, validation. Steven Wu: methodology. Jeremy P. Martin: cell culture, cell viability, cell immunolabeling. Kirati Tayutivutikul: cell culture, cell viability, cell immunolabeling. Guodong Du: methodology, supervision. Colin Combs: cell culture, cell viability, cell imaging. Diane C. Darland: conceptualization, methodology, supervision, review, funding support. Julia Xiaojun Zhao: conceptualization, methodology, supervision, review, funding support. All authors participated in editing the manuscript with Drs Zhao and Darland as co-corresponding authors.

Conflicts of interest

The authors declare no competing financial interest.

Acknowledgements

This work was supported by the NSF CHE 1709160 and NSF EPSCoR RII Track I Cooperative Agreement 1946202 (J. X. Z., G. D., and C. C.), NIH–COBRE on Epigenomics of Development and Disease 4P20GM104360-04 (J. P. M., K. T., and D. C. D.; R. Vaughan, PI), University of North Dakota Arts & Sci College 2022 Multi-investigator Seed Grants Initiative (J.X.Z. and D.C.D.). Imaging studies were conducted at the UND Imaging Core facility which is supported by NIH grant P20GM113123, DaCCoTA CTR NIH grant U54GM128729, and UNDSMHS funds.

References

1 C. Wu and D. T. Chiu, Highly Fluorescent Semiconducting Polymer Dots for Biology and Medicine, *Angew. Chem., Int. Ed.*, 2013, **52**(11), 3086–3109.
2 F. A. Villamena, Fluorescence Technique, in *Reactive Species Detection in Biology*, 2017, pp. 87–162.
3 H. Chen, L. Wu, Y. Wan, L. Huang, N. Li, J. Chen and G. Lai, One-step rapid synthesis of fluorescent silicon nanodots for a hydrogen peroxide-related sensitive and versatile assay based on the inner filter effect, *Analyst*, 2019, **144**(13), 4006–4012.
4 H. Sugimoto, M. Fujii, Y. Fukuda, K. Imakita and K. Akamatsu, All-inorganic water-dispersible silicon quantum dots: highly efficient near-infrared luminescence in a wide pH range, *Nanoscale*, 2014, **6**(1), 122–126.
5 H. Yanagawa, A. Inoue, H. Sugimoto, M. Shioi and M. Fujii, Antibody-conjugated near-infrared luminescent silicon quantum dots for biosensing, *MRS Commun.*, 2019, **9**(3), 1079–1086.

6 E. Abbasi, T. Kafshdooz, M. Bakhtiary, N. Nikzamir, N. Nikzamir, M. Nikzamir, M. Mohammadian and A. Akbarzadeh, Biomedical and biological applications of quantum dots, *Artif. Cells, Nanomed., Biotechnol.*, 2016, **44**(3), 885–891.

7 J. Geng, Z. Zhu, W. Qin, L. Ma, Y. Hu, G. G. Gurzadyan, B. Z. Tang and B. Liu, Near-infrared fluorescence amplified organic nanoparticles with aggregation-induced emission characteristics for *in vivo* imaging, *Nanoscale*, 2014, **6**(2), 939–945.

8 J. Huang and K. Pu, Near-infrared fluorescent molecular probes for imaging and diagnosis of nephro-urological diseases, *Chem. Sci.*, 2021, **12**(10), 3379–3392.

9 H. Li, Y. Kim, H. Jung, J. Y. Hyun and I. Shin, Near-infrared (NIR) fluorescence-emitting small organic molecules for cancer imaging and therapy, *Chem. Soc. Rev.*, 2022, **51**(21), 8957–9008.

10 H. M. Gil, T. W. Price, K. Chelani, J.-S. G. Bouillard, S. D. J. Calaminus and G. J. Stasiuk, NIR-quantum dots in biomedical imaging and their future, *iScience*, 2021, **24**(3), 102189.

11 M. M. Barroso, Quantum dots in cell biology, *J. Histochem. Cytochem.*, 2011, **59**(3), 237–251.

12 C. H. Chon and D. Li, Quantum Dot, in *Encyclopedia of Microfluidics and Nanofluidics*, ed. Li, D., Springer US, Boston, MA, 2008, pp. 1767–1769.

13 K. J. Klabunde and R. M. Richards, *Nanoscale Materials in Chemistry*, Wiley, 2009.

14 L. M. T. Phan, S. H. Baek, T. P. Nguyen, K. Y. Park, S. Ha, R. Rafique, S. K. Kailasa and T. J. Park, Synthesis of fluorescent silicon quantum dots for ultra-rapid and selective sensing of Cr(VI) ion and biomonitoring of cancer cells, *Mater. Sci. Eng., C*, 2018, **93**, 429–436.

15 H. D. Gliddon, P. D. Howes, M. Kaforou, M. Levin and M. M. Stevens, A nucleic acid strand displacement system for the multiplexed detection of tuberculosis-specific mRNA using quantum dots, *Nanoscale*, 2016, **8**(19), 10087–10095.

16 W. J. Parak, D. Gerion, T. Pellegrino, D. Zanchet, C. Micheel, S. C. Williams, R. Boudreau, M. A. L. Gros, C. A. Larabell and A. P. Alivisatos, Biological applications of colloidal nanocrystals, *Nanotechnology*, 2003, **14**(7), 15–27.

17 D. Li, X. Xu, P. Zhou, Y. Huang, Y. Feng, Y. Gu, M. Wang and Y. Liu, A facile synthesis of hybrid silicon quantum dots and fluorescent detection of bovine hemoglobin, *New J. Chem.*, 2019, **43**(48), 19338–19343.

18 R. Hardman, A toxicologic review of quantum dots: toxicity depends on physicochemical and environmental factors, *Environ. Health Perspect.*, 2006, **114**(2), 165–172.

19 F. Erogbogbo, J. May, M. Swihart, P. N. Prasad, K. Smart, S. E. Jack, D. Korcyk, M. Webster, R. Stewart, I. Zeng, M. Jullig, K. Bakeev, M. Jamieson, N. Kasabov, B. Gopalan, L. Liang, R. Hu, S. Schliebs, S. Villas-Boas and P. Gladding, Bioengineering silicon quantum dot theranostics using a network analysis of metabolomic and proteomic data in cardiac ischemia, *Theranostics*, 2013, **3**(9), 719–728.

20 A. Inoue, H. Sugimoto, H. Yaku and M. Fujii, DNA assembly of silicon quantum dots/gold nanoparticle nanocomposites, *RSC Adv.*, 2016, **6**(68), 63933–63939.

21 N. N. Greenwood and A. Earnshaw, 9–Silicon, in *Chemistry of the Elements*, ed. N. N. Greenwood and A. Earnshaw, Butterworth-Heinemann, Oxford, 2nd edn, 1997, pp. 328–366.

22 J. H. Warner, A. Hoshino, K. Yamamoto and R. D. Tilley, Water-Soluble Photoluminescent Silicon Quantum Dots, *Angew. Chem., Int. Ed.*, 2005, **44**(29), 4550–4554.

23 X. Cheng, R. Gondosiswanto, S. Ciampi, P. J. Reece and J. J. Gooding, One-pot synthesis of colloidal silicon quantum dots and surface functionalization *via* thiol–ene click chemistry, *Chem. Commun.*, 2012, **48**(97), 11874–11876.

24 Q. Li, T. Luo, M. Zhou, H. Abroshan, J. Huang, H. J. Kim, N. L. Rosi, Z. Shao and R. Jin, Silicon Nanoparticles with Surface Nitrogen: 90% Quantum Yield with Narrow Luminescence Bandwidth and the Ligand Structure Based Energy Law, *ACS Nano*, 2016, **10**(9), 8385–8393.

25 Y. He, Y. Zhong, F. Peng, X. Wei, Y. Su, Y. Lu, S. Su, W. Gu, L. Liao and S.-T. Lee, One-Pot Microwave Synthesis of Water-Dispersible, Ultraphoto- and pH-Stable, and Highly Fluorescent Silicon Quantum Dots, *J. Am. Chem. Soc.*, 2011, **133**(36), 14192–14195.

26 H. Sugimoto, M. Fujii, K. Imakita, S. Hayashi and K. Akamatsu, All-Inorganic Near-Infrared Luminescent Colloidal Silicon Nanocrystals: High Dispersibility in Polar Liquid by Phosphorus and Boron Codoping, *J. Phys. Chem. C*, 2012, **116**(33), 17969–17974.

27 J. Wang, D. Ye, G. Liang, J. Chang, J. Kong and J. Chen, One-step synthesis of water-dispersible silicon nanoparticles and their use in fluorescence lifetime imaging of living cells, *J. Mater. Chem. B*, 2014, **2**(27), 4338–4345.

28 F. Wu, X. Zhang, S. Kai, M. Zhang, H. Wang, J. N. Myers, Y. Weng, P. Liu, N. Gu and Z. Chen, One-Step Synthesis of Superbright Water-Soluble Silicon Nanoparticles with Photoluminescence Quantum Yield Exceeding 80, *Adv. Mater. Interfaces*, 2015, **2**(16), 1500360.

29 S. Ma, Y. Chen, J. Feng, J. Liu, X. Zuo and X. Chen, One-Step Synthesis of Water-Dispersible and Biocompatible Silicon Nanoparticles for Selective Heparin Sensing and Cell Imaging, *Anal. Chem.*, 2016, **88**(21), 10474–10481.

30 R. J. Clark, M. Aghajamali, C. M. Gonzalez, L. Hadidi, M. A. Islam, M. Javadi, M. H. Mobarok, T. K. Purkait, C. J. T. Robidillo, R. Sinelnikov, A. N. Thiessen, J. Washington, H. Yu and J. G. C. Veinot, From Hydrogen Silsesquioxane to Functionalized Silicon Nanocrystals, *Chem. Mater.*, 2017, **29**(1), 80–89.

31 S. P. Pujari, H. Driss, F. Bannani, B. van Lagen and H. Zuilhof, One-Pot Gram-Scale Synthesis of Hydrogen-Terminated Silicon Nanoparticles, *Chem. Mater.*, 2018, **30**(18), 6503–6512.

32 B. Sharma, S. Tanwar and T. Sen, One Pot Green Synthesis of Si Quantum Dots and Catalytic Au Nanoparticle–Si Quantum Dot Nanocomposite, *ACS Sustain. Chem. Eng.*, 2019, **7**(3), 3309–3318.

33 D. Roy, A. Mukhuty, C. Fouzder, N. Bar, S. Chowdhury, R. Kundu and P. Chowdhury, Multi-emissive biocompatible silicon quantum dots: Synthesis, characterization, intracellular imaging and improvement of two fold drug efficacy, *Dyes Pigm.*, 2021, **186**, 109004.

34 M. Sakiyama, H. Sugimoto and M. Fujii, Long-lived luminescence of colloidal silicon quantum dots for time-gated fluorescence imaging in the second near infrared window in biological tissue, *Nanoscale*, 2018, **10**(29), 13902–13907.

35 M. Fujii, A. Minami and H. Sugimoto, Precise size separation of water-soluble red-to-near-infrared-luminescent silicon quantum dots by gel electrophoresis, *Nanoscale*, 2020, **12**(16), 9266–9271.

36 M. Fujii, R. Fujii, M. Takada and H. Sugimoto, Silicon Quantum Dot Supraparticles for Fluorescence Bioimaging, *ACS Appl. Nano Mater.*, 2020, **3**(6), 6099–6107.

37 C. M. Hessel, E. J. Henderson and J. G. C. Veinot, Hydrogen Silsesquioxane: A Molecular Precursor for Nanocrystalline Si−SiO2 Composites and Freestanding Hydride-Surface-Terminated Silicon Nanoparticles, *Chem. Mater.*, 2006, **18**(26), 6139–6146.

38 A. N. Thiessen, L. Zhang, A. O. Oliynyk, H. Yu, K. M. O'Connor, A. Meldrum and J. G. C. Veinot, A Tale of Seemingly "Identical" Silicon Quantum Dot Families: Structural Insight into Silicon Quantum Dot Photoluminescence, *Chem. Mater.*, 2020, **32**(16), 6838–6846.

39 D. C. Darland, J. T. Cain, M. A. Berosik, M. Saint-Geniez, P. W. Odens, G. J. Schaubhut, S. Frisch, A. Stemmer-Rachamimov, T. Darland and P. A. D'Amore, Vascular endothelial growth factor (VEGF) isoform regulation of early forebrain development, *Dev. Biol.*, 2011, **358**(1), 9–22.

40 J. T. Cain, M. A. Berosik, S. D. Snyder, N. F. Crawford, S. I. Nour, G. J. Schaubhut and D. C. Darland, Shifts in the vascular endothelial growth factor isoforms result in transcriptome changes correlated with early neural stem cell proliferation and differentiation in mouse forebrain, *Dev. Neurobiol.*, 2014, **74**(1), 63–81.

41 W. H. Melhuish, Quantum Efficiencies of Fluorescence of Organic Substances: Effect of Solvent and Concentration of the Fluorescent Solute, *J. Phys. Chem.*, 1961, **65**(2), 229–235.

42 S. Reagen, Y. Wu, X. Liu, R. Shahni, J. Bogenschuetz, X. Wu, Q. R. Chu, N. Oncel, J. Zhang, X. Hou, C. Combs, A. Vasquez and J. X. Zhao, Synthesis of Highly Near-Infrared Fluorescent Graphene Quantum Dots Using Biomass-Derived Materials for *In Vitro* Cell Imaging and Metal Ion Detection, *ACS Appl. Mater. Interfaces*, 2021, **13**(37), 43952–43962.

43 B. Strehmel, C. Schmitz, C. Kütahya, Y. Pang, A. Drewitz and H. Mustroph, Photophysics and photochemistry of NIR absorbers derived from cyanines: key to new technologies based on chemistry 4.0, *Beilstein J. Org. Chem.*, 2020, **16**, 415–444.

44 E. I. Shramova, A. B. Kotlyar, E. N. Lebedenko, S. M. Deyev and G. M. Proshkina, Near-infrared activated cyanine dyes as agents for photothermal therapy and diagnosis of tumors, *Acta Naturae*, 2020, **12**(3), 102–113.

45 M. K. Rasmussen, J. N. Pedersen and R. Marie, Size and surface charge characterization of nanoparticles with a salt gradient, *Nat. Commun.*, 2020, **11**(1), 2337.

46 X. Liu, IR Spectrum and Characteristic Absorption Bands, in *Organic Chemistry I*, Kwantlen Polytechnic University, 2023.

47 J. Wu, J. Dai, Y. Shao and Y. Sun, One-step synthesis of fluorescent silicon quantum dots (Si-QDs) and their application for cell imaging, *RSC Adv.*, 2015, **5**(102), 83581–83587.

48 C. Wang, G. Zhou, Y. Li, N. Lu, H. Song and L. Zhang, Biocatalytic esterification of caprylic acid with caprylic alcohol by immobilized lipase on amino-functionalized mesoporous silica, *Colloids Surf., A*, 2012, **406**, 75–83.

49 S. Bose, M. A. Ganayee, B. Mondal, A. Baidya, S. Chennu, J. S. Mohanty and T. Pradeep, Synthesis of Silicon Nanoparticles from Rice Husk and their Use as Sustainable Fluorophores for White Light Emission, *ACS Sustain. Chem. Eng.*, 2018, **6**(5), 6203–6210.

50 J. Chen, X. Wu, X. Hou, X. Su, Q. Chu, N. Fahruddin and J. X. Zhao, Shape-Tunable Hollow Silica Nanomaterials Based on a Soft-Templating Method and Their Application as a Drug Carrier, *ACS Appl. Mater. Interfaces*, 2014, **6**(24), 21921–21930.

51 Y. Jin, A. Li, S. G. Hazelton, S. Liang, C. L. John, P. D. Selid, D. T. Pierce and J. X. Zhao, Amorphous silica nanohybrids: Synthesis, properties and applications, *Coord. Chem. Rev.*, 2009, **253**(23), 2998–3014.

52 A. Shiohara, S. Hanada, S. Prabakar, K. Fujioka, T. H. Lim, K. Yamamoto, P. T. Northcote and R. D. Tilley, Chemical Reactions on Surface Molecules Attached to Silicon Quantum Dots, *J. Am. Chem. Soc.*, 2010, **132**(1), 248–253.

53 L. Pavesi, L. Dal Negro, C. Mazzoleni, G. Franzò and F. Priolo, Optical gain in silicon nanocrystals, *Nature*, 2000, **408**(6811), 440–444.

54 J. D. Holmes, K. J. Ziegler, R. C. Doty, L. E. Pell, K. P. Johnston and B. A. Korgel, Highly Luminescent Silicon Nanocrystals with Discrete Optical Transitions, *J. Am. Chem. Soc.*, 2001, **123**(16), 3743–3748.

55 K. Dohnalová, A. N. Poddubny, A. A. Prokofiev, W. D. A. M. de Boer, C. P. Umesh, J. M. J. Paulusse, H. Zuilhof and T. Gregorkiewicz, Surface brightens up Si quantum dots: direct bandgap-like size-tunable emission, *Light: Sci. Appl.*, 2013, **2**(1), e47.

56 D. Beri, Silicon quantum dots: surface matter, what next?, *Adv. Mater.*, 2023, **4**(16), 3380–3398.

57 C. A. Schneider, W. S. Rasband and K. W. Eliceiri, NIH Image to ImageJ: 25 years of image analysis, *Nat. Methods*, 2012, **9**(7), 671–675.

58 S. Ohta, K. Yamura, S. Inasawa and Y. Yamaguchi, Aggregates of silicon quantum dots as a drug carrier: selective intracellular drug release based on pH-responsive aggregation/dispersion, *Chem. Commun.*, 2015, **51**(29), 6422–6425.

59 X. Cheng, B. F. P. McVey, A. B. Robinson, G. Longatte, P. B. O'Mara, V. T. G. Tan, P. Thordarson, R. D. Tilley, K. Gaus and J. J. Gooding, Protease sensing using nontoxic silicon quantum dots, *J. Biomed. Opt.*, 2017, **22**(8), 1–7.